

Title: Emergence of Anti-chemotactic Flocking in Active Biomimetic Colloids

Authors: Joseph D. Lopes^{1,*}, Benjamin Winterstrain^{1,*}, Fernando Caballero¹, Amélie Chardac¹, Izaiah Alvarado², Adrielle T. Cusi¹, Shibani Dalal¹, Gess Kelly¹, Michael R. Stehnach¹, Bruce L. Goode³, Thomas G. Fai⁴, Michael F. Hagan¹, Michael M. Norton¹, Guillaume Duclos^{1,†}

Affiliations: ¹Department of Physics, Brandeis University, Waltham, MA 02453; ²Department of Biochemistry, Brandeis University, Waltham, MA 02453; ³Department of Biology, Brandeis University, Waltham, MA 02453; ⁴Department of Mathematics, Brandeis University, Waltham, MA 02453; *authors contributed equally.†gduclos@brandeis.edu

Abstract

Competition for resources is a fundamental constraint that guides the self-organization of natural, biological, and human systems, ranging from urban planning and ecosystem development to intracellular pattern formation. Here, we reveal that competition for resources is at the origin of the collective dynamics that emerge in a population of colloids propelled by actin treadmilling, an out-of-equilibrium process where filaments grow from one end while shrinking from the other. Using a combination of experiments and theory, we show that symmetry-breaking, self-propulsion, and flocking emerge from the local competition for actin monomers. We demonstrate that beads propelled by actin treadmilling are anti-chemotactic and spontaneously generate asymmetric actin gradients that trigger and sustain directed motility. Flocking emerges from the combined effects of anti-chemotaxis and local competition for monomers. The flocking transition depends on the actin polymerization rate, actin monomer diffusivity, and the bead's motility, whose interplay controls the emergence of short-range attractive interactions between the colloids. Our findings demonstrate that active stress generation coupled to reaction-diffusion is a generic mechanism that can lead to a multiscale cascade of behaviors when active agents remodel their environment. Actin treadmilling offers a platform to study how motile agents that interact through a field self-organize in novel dynamical phases, with potential applications in non-reciprocal and trainable active matter.

Introduction

Pattern formation via reaction-diffusion is a ubiquitous organizational principle in nature, from ecological niche organization [1-4] and oscillatory chemical reactions [5-7] to cytokinesis in microbiology [8, 9] and embryogenesis [10, 11]. In his seminal paper "The Chemical Basis of Morphogenesis", Alan Turing showed that coupled reaction-diffusion equations of two chemical species - one activator and one inhibitor - can lead to spontaneous symmetry breaking and pattern formation [12]. Turing, however, explicitly left out the coupling between chemistry and mechanical stresses from his morphogenesis theory. Recent theory [13] and experimental work [14] started to address this knowledge gap, showing, for example, that the coupling between reaction-diffusion and stress generation governs the establishment of polarization in embryogenesis [15]. Actin, specifically, one of the most abundant proteins in the cell cytoplasm,

responsible for cell contractility and motility, has been shown to behave as a chemo-mechanical excitable medium [16-21].

Biomolecular active matter composed of purified proteins provides a route towards building materials with chemo-mechanical feedback that mimics defining features of morphogenesis [22]. To date, most experimental research in this field has focused on materials homogeneously driven out of equilibrium by molecular motors [23-25]. Recent experiments with externally applied ATP gradients [26] or light-activable molecular motors [27, 28] have revealed how spatiotemporally heterogeneous activity impacts transport and spontaneous flows. The impact of activity gradients generated by internal, self-organized processes remains largely unexplored. This is particularly relevant during development, where protein patterns are ubiquitous, or, more generally, in cases where the active motile agents are competing for resources [29-31] or remodel their environment [32-37].

Cells use multiple mechanisms to transduce chemical energy into mechanical work without molecular motors, including treadmilling, where filaments polymerize at one end while depolymerizing at the other. Treadmilling polymers drive a variety of physiological processes across the tree of life [38, 39]. Motility driven by actin treadmilling is ubiquitous in biology; the dynamical process is used in cell lamellipodia [40], hijacked by parasites like *Listeria*, *Shigella* [41, 42], as well as viruses [43]. Actin treadmilling can even propel intracellular organelles such as mitochondria [44]. Theory, computer simulations, and experiments have shown that the interplay between treadmilling and elasticity can explain various aspects of this mode of motility, from symmetry breaking [45-48] and intermittent motion [49] to corkscrew swimming patterns [50]. However, treadmilling dynamics become more complex in non-homogeneous environments. Local competition for actin monomers can slow down and even steer network growth [29]. More recently, it has been reported that global competition for a limited pool of actin can also affect actin network growth and structure [30].

Here, we unravel how the chemomechanical coupling between non-equilibrium actin turnover, reaction-diffusion, and motility promotes the emergence of collective flocking dynamics of micron-sized colloids propelled by treadmilling actin comet tails [42, 51, 52]. We show that our artificial *Listeria* interact through actin monomer gradients, created by the consumption of monomers needed for their self-propulsion. The actin comets are effectively anti-chemotactic. Local depletion of monomeric actin between two beads creates local gradients in the polymerization rate, which result in an effective attraction and, subsequently, flocking. We propose a simple reaction-diffusion model in which actin polymerization exerts an extensile active stress normal to the bead surface. This model captures all the experimental phenomenology, including spontaneous symmetry breaking, motility, actin concentration profiles, and flocking. Combining experiments and theory, we show that flocking is suppressed when the diffusivity dominates over the reaction rate. Finally, in 3D, motile beads accumulate along walls, but not along porous boundaries, a consequence of the asymmetric self-generated gradient near impermeable boundaries. Our findings establish actin turnover as a promising experimental platform for engineering collective behavior and pattern formation in chemomechanical molecular materials.

Main

Beads propelled by actin comets exhibit flocking behavior influenced by steric interactions.

We investigate the motion of colloidal particles propelled by actin treadmilling, a well-established model system inspired by microbial pathogens such as *Listeria* and *Shigella*, which use actin-based motility to move intracellularly and spread from cell to cell [42, 51, 52]. In brief, we coated micron-sized polystyrene beads with pVCA, the domain of the human N-WASP protein that activates Arp2/3 complex to nucleate the formation of branched actin networks [53]. A homogenous coat of pVCA on the bead surface nucleates an actin shell, which spontaneously breaks symmetry and propels the bead forward (**Fig. 1A-C**). While new actin filaments continue to be nucleated and grow the network at the end closest to the bead surface, a mixture of actin-binding proteins sever and depolymerize the older filaments at the trailing end of the network, replenishing the global monomer pool (**Fig. S1**, materials and methods).

In these experiments, we confined the motile beads between two coverslips. The diameter of the beads ranged from 1.5 to 10 μm , and the height of the chamber was chosen to enforce steric interactions (**Fig. S2**), creating a quasi-2D chamber whose thickness was less than two bead diameters (**Fig. 1A**). Binary collisions between motile beads revealed that the beads realign upon collision and have polar aligning interactions (**Fig. S2C**). These collisions led to rich flocking dynamics (**Fig. 1D-E**, **Movies S1, S2**). Flocks had a finite size, ranging from two beads to tens of beads (**Fig. 1I**, **Fig. S3**) and a stereotypical “U” shape, with exterior beads slightly ahead of those on the flock’s interior. Flocks constantly merged and broke apart as individual beads and flocks collided, resulting in highly dynamic finite-size flocks (**Fig. 1J-K**).

To quantify the degree of flocking, we tracked and grouped motile beads into flocks if they satisfied distance and velocity vector alignment thresholds (see Materials and methods). We then defined a flocking parameter Q_f as the fraction of motile beads that belonged to a flock. In the flocking phase, 40-60% of the beads belonged to a flock. This metric helped identify the experimental conditions that promote flocking (**Fig. 1H**). We found that the quasi-2D confinement was necessary but not sufficient to promote flocking: when the chamber thickness was larger than two beads’ diameters, colliding beads did not flock because they could move on top of each other and not reorient upon collision (**Fig. S2**). Flocking also disappeared despite the quasi-2D confinement when bead diameter was decreased: beads were motile, reorienting upon collision, but did not flock (**Fig. 1F-G**, **Fig. S4**, **Movies S3,S4**). For the remainder of this study, we focus on unraveling the origin of this flocking transition.

Spontaneous symmetry breaking and motility emerge in a reaction-diffusion model coupled to active stress generation.

We hypothesized that flocking results from the competition for actin monomers, where the non-uniform monomer distribution around neighboring beads leads to polymerization rate gradients that drive beads together into stable flocks (**Fig. 1L-M**). Resource competition is corroborated by measurements of beads’ speed and actin tail length, which decrease systematically with local bead density (**Fig. S5**, see SI for other hypotheses we considered).

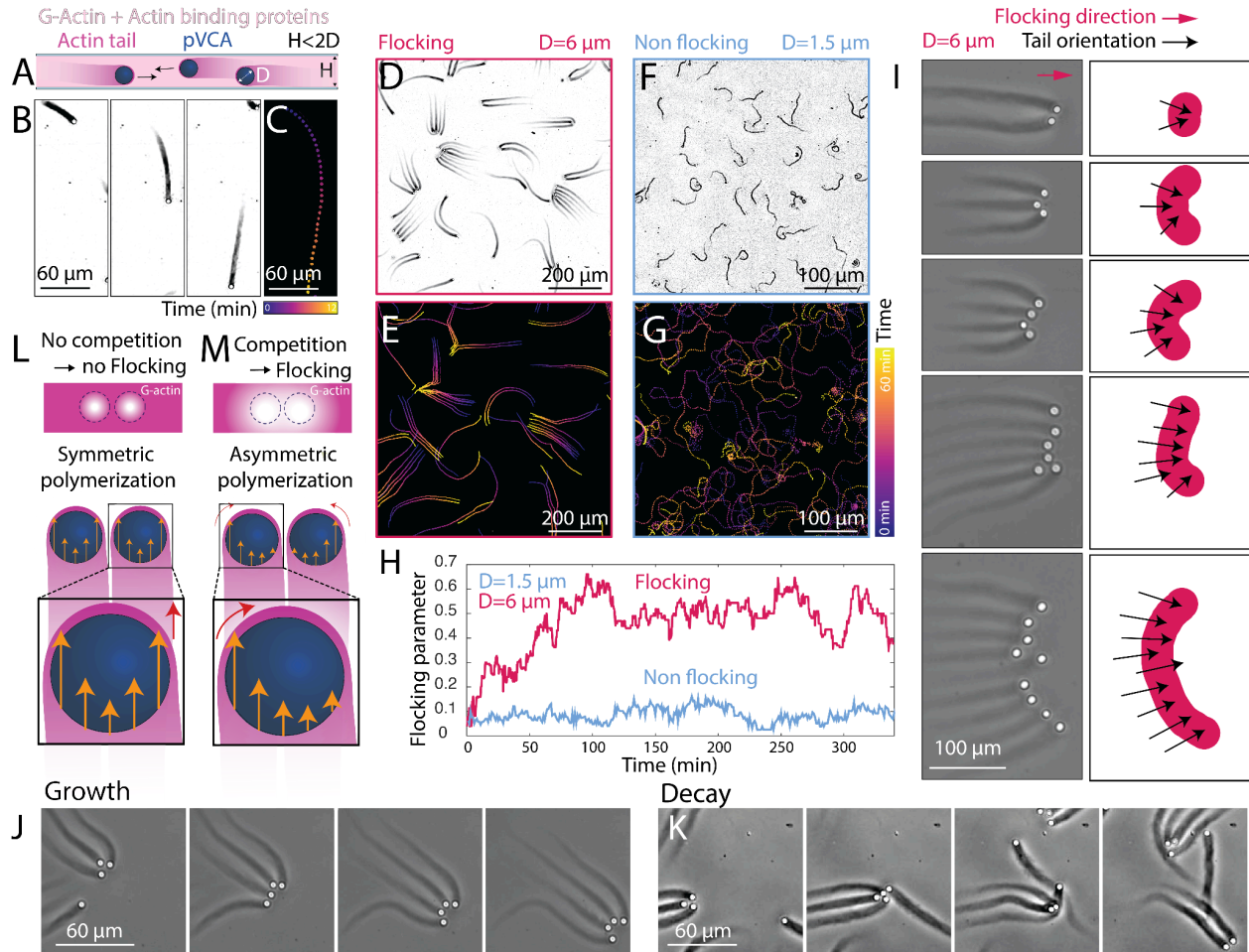


Fig. 1: Flocking of motile beads propelled by actin treadmilling. A) Side view schematic of the experiment. Beads are covered with pVCA and suspended in a solution containing actin monomers (G-actin), ATP, and actin-binding proteins. B) Time series of a motile bead (5 min between each frame, $D=6 \mu\text{m}$). C) Color-coded position of the bead shown in B. D) Flocking beads ($D=6 \mu\text{m}$). E) Color-coded trajectories of the flocking beads shown in D. F) Non-flocking beads ($D=1.5 \mu\text{m}$). G) Color-coded trajectories of the non-flocking beads shown in F. H) Temporal evolution of the flocking parameter (fraction of flocking beads in a Field of View) for flocking ($D=6 \mu\text{m}$) and non-flocking ($D=1.5 \mu\text{m}$) beads. I) Snapshots of flocks of varying sizes. The flocks have a stereotypical “U” shape. J) Time series of motile beads merging with a flock. The flock size increases (7 min between each frame). K) Time series of motile beads colliding with and disrupting a flock. The flock size decreases (7 min between each frame). L-M) Model for how competition for actin monomers could lead to asymmetric polymerization rates on each bead and flocking. Orange arrows indicate relative actin polymerization rates on the bead surface. Red arrows indicate the direction of bead movement.

Inspired by previous works on cell motility [54-56], we propose a chemomechanical reaction-diffusion phase field model (Fig. 2A) that captures the hallmarks of the actin comet assay: spontaneous motility and flocking [54-56]. We modeled the spatiotemporal dynamics of actin monomers c_m and their incorporation into a polymerized tail c_p through a simplified version

of the reaction chemistry. The polymerization rate R_{on} was modeled as a two-stage nucleation and growth process with rates, k_1 and k_2 , respectively.

$$R_{on} = c_m \left(k_1 + \frac{k_2 c_p^2}{c_p^2 + k_d^2} \right).$$

We assumed that polymerization obeys a Hill function in c_p , which captures both the cooperative nature of polymerization and saturation of the reaction rate [54]. Each bead was described by a distinct phase field $\phi_i(r, t)$. We used the following coupled transport equations for monomeric and polymerized actin:

$$\begin{aligned} \partial_t c_m &= D_m \nabla^2 \frac{\delta F_c}{\delta c_m} - R_{on} \sum |\nabla \phi_i|^2 + k_{off} c_p \\ \partial_t c_p &= D_p \nabla^2 \frac{\delta F_c}{\delta c_p} + R_{on} \sum |\nabla \phi_i|^2 - k_{off} c_p, \end{aligned}$$

where polymerization was localized to the surface of the phase fields $\phi_i(r, t)$. The last term proportional to k_{off} accounts for actin depolymerization. Dynamics of the beads' phase fields are given by $\partial_t \phi_i + \mathbf{u} \cdot \nabla \phi_i = - \frac{\delta F}{\delta \phi_i}$, where the free energy F describes the preferred morphology of the phase field [56] (See supplementary materials for the full equation for the phase field).

The flow field \mathbf{u} responsible for advecting the beads is described by the overdamped and incompressible Stokes equation:

$$\sum_{i=1}^N \nabla \cdot \left[- \left(\alpha R_{on} + \Gamma \right) \nabla \phi_i \otimes \nabla \phi_i \right] + \nabla^2 \mathbf{u} - \epsilon^2 \mathbf{u} - \nabla P = 0.$$

where the positive prefactor α scales the polymerization rate R_{on} introduced earlier, Γ is a ratio of dissipation rates, ϵ^{-1} is the screening length resulting from substrate dissipation, and P is the hydrostatic pressure enforcing continuity (see SI for a full derivation of the equations). We solved the system of coupled partial differential equations using the publically available software cuPPs [57].

We modeled the force generated by polymerization as an extensile stress oriented perpendicular to the surface - i.e. parallel to $\nabla \phi_i$, when $\alpha > 0$ - and with a strength proportional to the polymerization rate R_{on} (**Fig. 2A**). This effective active stress coarse-grains details of the actin polymerization ‘‘ratchet’’, allowing us to readily couple mass transport and active force generation [47, 48]. Consequently, activity appears as an augmented (additional) surface tension, wherein reaction rate gradients lead to concomitant changes in local surface tension that drive bead motion. Thus, at the level of our continuum model, the propulsion is analogous to a Marangoni flow. Qualitatively, the net effect of the active term is the creation of a ‘‘squeezing’’ stress on the trailing edge of the colloids, commensurate with previous studies [58]. Both the passive and active surface stresses were summed over all beads.

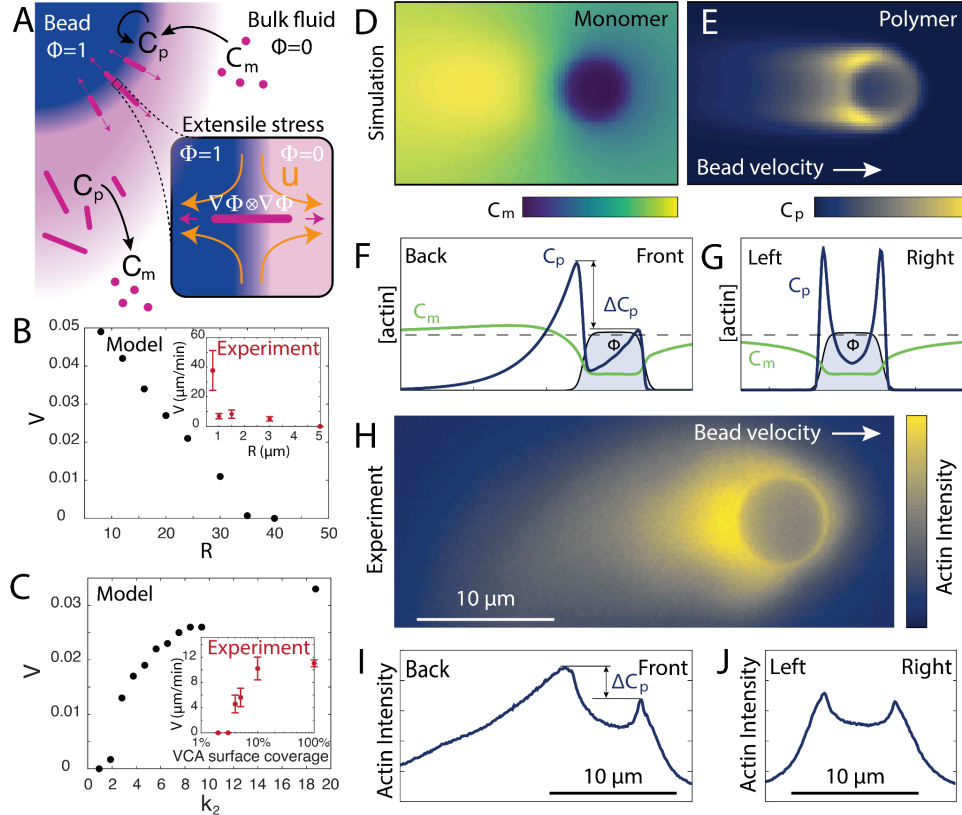


Fig. 2: Symmetry breaking and self-propulsion in a chemomechanical reaction-diffusion model where actin polymerization generates extensile active stresses. A) Schematic of the chemomechanical reaction-diffusion model. The bead is described by a phase field Φ . Polymerization at the boundary of the phase field generates an extensile stress normal to the boundary. B) Self-propulsion speed as a function of the phase field's radius R . Inset: experimentally measured speed as a function of the beads' radius. C) Self-propulsion speed as a function of non-linear polymerization rate k_2 . Inset: experimentally measured speed as a function of the surface coverage of branched actin nucleator factor pVCA. D) actin monomer and E) polymer fields of a simulated motile bead after symmetry breaking. F) Back-Front and G) Left-right profiles of the monomer (green) and polymer field (blue). The back-front profile is asymmetric and the back of the bead is enriched in actin. The left-right profile is symmetric. The monomeric field increases exponentially from the bead surface. H) Fluorescent image of the actin tail. I) Back-front and J) left-right profile of the actin around a motile bead.

This model captures all the hallmarks of the actin comet motility. First, the coupling between reaction and motility led to a spontaneous symmetry breaking that propelled the bead forward (**Movie S5**). Second, increasing bead size led to a decrease in the self-propulsion speed (**Fig. 2B**, **Movie S6**) and eventually inhibited symmetry breaking, which are both consistent with our experiments (**Fig. 2B Inset**). Third, the self-propulsion speed increased and plateaued as the non-linear growth rate k_2 increased (**Fig. 2C**, **Movie S7**), consistent with experiments in which the surface coverage of pVCA was increased (**Fig. 2C Inset**). Once the actin shell broke symmetry and the bead reached a steady state velocity, both the monomer and the polymer

concentrations were enriched at the trailing edge of the phase field bead (**Fig. 2D-G**), consistent with the actin profiles measured experimentally (**Fig. 2H-J**).

The flocking transition is controlled by short-range attractive interactions.

Increasing the number of beads in the simulation allowed us to identify the mechanisms that control the flocking transition. The complex interplay between reaction, diffusion, and motility leads to short-range attractive interactions between beads. Two motile beads propelling towards each other will slow down and reorient their self-propulsion towards each other (**Fig. 3A-C**). The effective attraction is associated with a left/right asymmetric profile of monomeric actin around each bead that results from the local depletion of actin monomers between the two beads (**Fig. 3D**). Flocking is apparent when the particle density is increased (**Fig. 3E, Movie S8**). The flocks have the same stereotypical “U” shape as in the experiments (**Fig. 3F-G, Fig 1I**). Changing R , the bead’s radius, and D_m , the actin monomer’s diffusivity, revealed three distinct active phases: flocking, non-flocking, and non-motile beads (**Fig. 3H**). Flocking disappears when the actin monomer’s diffusivity is increased (**Fig. 3H, Movie S9**). The flocking/non-flocking phase boundary is non-monotonic with bead radius, consistent with the experimental result that flocking is suppressed for small beads (**Fig. 1F-H**). We also note that increasing the non-linear growth rate k_2 leads to an expansion of the flocking regime in the (D_m, R) phase space (**Fig. S6A**). The activity α has a nonlinear effect on the transition, as increasing α promotes, but then inhibits, flocking (**Fig. S6B**).

To understand these results, we performed simulations with a single motile bead, and measured the exponential decay length ξ associated with the short-range gradient of actin monomers perpendicular to the direction of motion (left/right axis of the actin comet, c_m in **Fig. 2G**). We show that this short-range actin gradient depends on the reaction rate on the bead surface and the diffusivity of the monomers: faster monomer diffusion erases gradients far from the particle while faster reaction rates compete against this diffusion, creating a wider and deeper sink in the monomer concentration. The decay length ξ increased when increasing the non-linear growth rate k_2 (**Fig. 4A,D**), decreased when increasing the diffusivity of actin monomers (**Fig. 4B,E**), and evolved non-monotonically with particle radius (**Fig. 4C,F**). We systematically observed that motile beads were flocking when the monomeric decay length ξ was larger than W , the thickness of the phase field interface (**Fig. 4D-F**). To be more quantitative, we rescaled all the data points from about 100 independent simulations with $N=3$ beads onto a single 1D phase diagram with ξ/W as a control parameter. All the data points collapsed into three distinct regions with the phase boundary between the flocking and non-flocking phases corresponding to $\xi/W = 1$ (**Fig. S7, dashed line in Fig. 3H**). This measurement suggests that neighboring beads respond to each other’s self-generated gradients and flock when the short-range actin gradient extends further than the phase field surface.

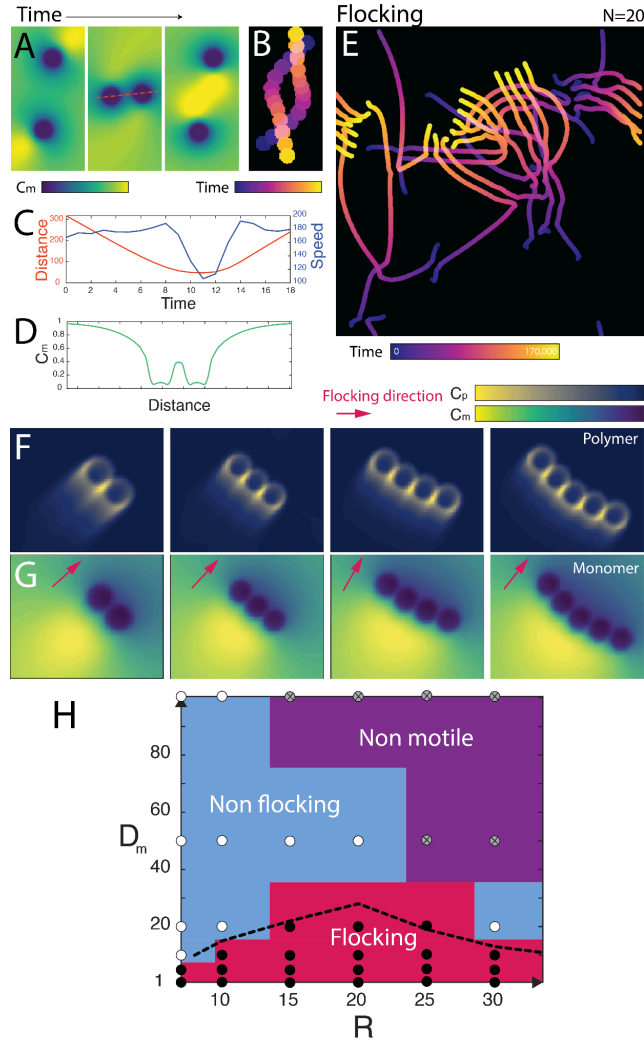


Fig. 3: Flocking in a reaction-diffusion model coupled to active stress generation. A) Time series of two beads moving towards each other and reorienting (monomer field is color-coded). B) Color-coded trajectory of the beads shown in A. C) Temporal evolution of the speed and the distance between the two beads suggests the existence of short-range attractive interactions. D) Profile of monomeric actin along the dashed line shown in A. As the beads reorient, the monomeric actin profile around each bead is asymmetric. E) Color-coded trajectories of $N=20$ beads. The beads flock. F-G) Examples of flocks of different sizes found in the simulations. F) polymer field and G) monomer fields around the flocks. The flocking direction is indicated with a red arrow. H) Phase diagram where the actin monomer diffusivity D_m and the droplet's radius R are changed. Each data point represents a different simulation with $N=3$ droplets. The dashed line represents the flocking/non-flocking phase boundary where $\xi/W=1$.

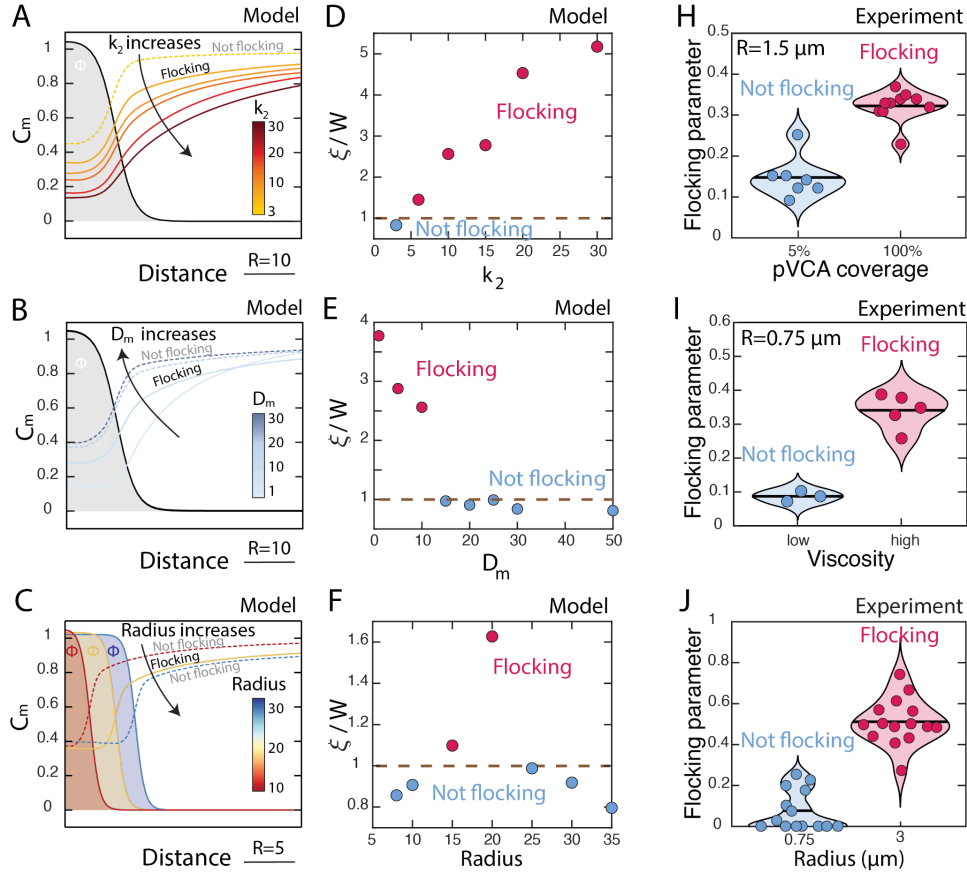


Fig. 4: The flocking transition is controlled by short-range attractive interactions. A-C) Actin monomer profiles along the left-right axis of isolated motile beads where A) the non-linear growth rate k_2 , B) the actin monomer diffusivity D_m , and C) the droplet's radius R are increased. D-F) Ratio of ξ , the characteristic length of the short-range actin monomer gradient around a motile bead, and W , the thickness of the phase field boundary, as a function of D) the non-linear growth rate k_2 , E) the actin monomer diffusivity D_m , and F) the droplet's radius. Data points are labeled as flocking or non-flocking depending on the collective behaviors observed for $N=3$ beads (**Fig. 3H** and **Fig. S6**). H-J) Flocking parameter in experiments in which H) the surface coverage of actin nucleator (pVCA protein), I) the viscosity of the solution, and J) the radius of the beads are increased. Each data point corresponds to a distinct independent experiment. The continuous black line represents the mean flocking parameter averaged over all the replicates.

We found striking agreement between the experiments and the theory regarding the impact of the polymerization rate k_2 , actin diffusivity D_m , and bead size R on the flocking transition. Decreasing the growth rate k_2 by decreasing the surface coverage of the actin nucleation factor (pVCA) led to a transition from a flocking to a non-flocking phase (**Fig. 4H**). Adding a high molecular weight non-absorbing polymer (see Materials and methods) increased the viscosity of the surrounding fluid and decreased monomer diffusivity D_m , leading to a transition from a non-flocking to a flocking phase (**Fig. 4I**). Finally, decreasing the size of the beads led to a

transition from a flocking to a non-flocking phase (**Fig. 5J**). Systematic agreement between these observations and model predictions strongly supports that the spatial distribution of monomers is the primary driver of bead-bead interactions.

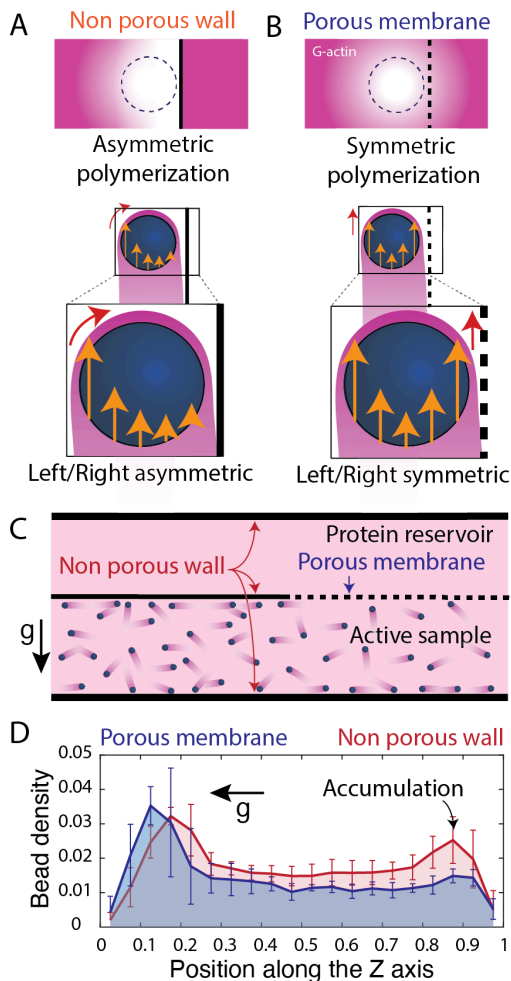


Fig. 5: Asymmetric self-generated gradients and antichemotaxis lead to accumulation against solid (non-porous) boundaries. A-B) Schematic representation of motile beads moving along A) a solid, non-porous wall and B) a porous membrane connected to a reservoir of proteins. C) Schematic representation of a side view of the experimental setup. The motile beads are in a 200 μm -thick microfluidic chamber. The top wall of that chamber is either a non-porous wall or a porous membrane connected to a protein reservoir. D) Density of active beads measured along the Z direction using confocal microscopy. We detect a strong accumulation of motile beads along the non-porous wall (red curve) and no accumulation along the porous membrane (blue curve). The dark continuous lines show the average, and the errorbars show the standard deviation for $N=3$ (porous membrane) and $N=5$ (non-porous wall) independent replicates.

Accumulation of motile beads along solid (non-porous) boundaries.

The reaction-diffusion mediated interactions at the origin of the flocking transition in quasi-2D geometry also have consequences in 3D. Indeed, we expect that motile beads in 3D will also

remodel the actin monomer landscape. In particular, motile beads near a wall should generate an asymmetric gradient of monomers that produces an effective attraction to the wall (**Fig. 5A**). However, if the boundary is instead porous and connected to a protein reservoir, a bead swimming along a wall should generate a symmetric actin gradient, eliminating this attraction (**Fig. 5B**). We confirmed this hypothesis by performing experiments in a thick microfluidic chamber (**Fig. S8**) whose upper wall was either a non-porous boundary, or a porous membrane connected to a protein reservoir with actin, ATP, and all the other actin-binding proteins (**Fig. 5C**). First, we noted that beads can swim in 3D, demonstrating that interactions with a surface are not necessary for them to propel. Second, we measured the density profile along the transverse direction and confirmed that beads accumulated on non-porous walls, and significantly less on porous boundaries (**Fig. 5D**). These results confirm that beads sense and respond to self-generated actin gradients both in quasi-2D geometries and in 3D.

Conclusion

Our experiments and theory showed that the chemomechanical interplay between non-equilibrium actin turnover and motility leads to flocks stabilized by self-generated monomer gradients. Beads compete for resources, and the resulting coupling through the monomer field gives rise to novel flock morphologies unseen in sterically interacting particles [59], swimmers [60], as well as Marangoni swimmers that similarly interact through concentration fields [34, 61]. Omitting the details of the elastic actin shell in favor of an effective active stress in our model captures the essential coupling between actin polymerization and motility, driving spontaneous motion and anti-chemotactic flocking. *In vivo*, the cytoskeleton is a dynamic, self-regulating material whose constitutive building blocks continuously turn over, coming in and out of the self-organized structure. Replicating this functionality in synthetic systems reveals fundamental principles underlying intracellular self-organization. In the future, incorporating additional regulatory networks that control actin dynamics will certainly offer exciting opportunities to build self-regulating materials, non-reciprocally interacting active machines [62], or materials that learn novel dynamical behaviors [63] from the bottom up. By bridging reaction-diffusion and active mechanics, two hallmarks of morphogenesis, our work establishes non-equilibrium turnover as a fundamental process to build a novel class of active materials that mimic essential chemomechanical feedback found in cells and developing embryos.

Data availability

All data reported in the main text and supplementary information as well as executable code for numerical simulations will be made available on Dryad.

Acknowledgement

All the experimental work, data analysis, and early version of the model was supported by the U.S. Department of Energy (DOE), Office of Science, Basic Energy Sciences (BES) under Award # DE-SC0024120. Computational work was supported by the Brandeis University NSF MRSEC under Award # DMR 2011846. B.L.G. acknowledges support from NIH (R35 GM134895). We thank members of the Goode lab for providing purified actin and actin-binding proteins in the early stages of this study and for teaching the authors how to purify these proteins. We also acknowledge the use of the optical, microfluidics, and biomaterial facilities

supported by NSF MRSEC Grant No. DMR-2011846. We acknowledge computational support from NSF XSEDE computing resources allocation Grant No. TG-MCB090163 and the Brandeis HPCC, which is partially supported by the NSF through Grants No. NSF-DMR-MRSEC-2011846 and No. OAC-1920147.

Reference list

1. Lotka, A.J., *Contribution to the Theory of Periodic Reactions*. The Journal of Physical Chemistry, 1910. **14**(3): p. 271-274.
2. Touboul, J.D., A.C. Staver, and S.A. Levin, *On the complex dynamics of savanna landscapes*. Proceedings of the National Academy of Sciences, 2018. **115**(7): p. E1336-E1345.
3. Rietkerk, M., et al., *Evasion of tipping in complex systems through spatial pattern formation*. Science, 2021. **374**(6564): p. eabj0359.
4. Weiner, B.G., A. Posfai, and N.S. Wingreen, *Spatial ecology of territorial populations*. Proceedings of the National Academy of Sciences, 2019. **116**(36): p. 17874-17879.
5. Lotka, A.J., *Analytical Note on Certain Rhythmic Relations in Organic Systems*. Proc Natl Acad Sci U S A, 1920. **6**(7): p. 410-5.
6. Zhabotinsky, A.M., *Periodical oxidation of malonic acid in solution (a study of the Belousov reaction kinetics)*. Biofizika, 1964. **9**: p. 306-311.
7. Bánsági, T., V.K. Vanag, and I.R. Epstein, *Tomography of Reaction-Diffusion Microemulsions Reveals Three-Dimensional Turing Patterns*. Science, 2011. **331**(6022): p. 1309-1312.
8. Huang, K.C., Y. Meir, and N.S. Wingreen, *Dynamic structures in Escherichia coli: spontaneous formation of MinE rings and MinD polar zones*. Proc Natl Acad Sci U S A, 2003. **100**(22): p. 12724-8.
9. Loose, M., et al., *Spatial Regulators for Bacterial Cell Division Self-Organize into Surface Waves in Vitro*. Science, 2008. **320**(5877).
10. Bement, W.M., et al., *Activator–inhibitor coupling between Rho signalling and actin assembly makes the cell cortex an excitable medium*. Nature Cell Biology, 2015. **17**(11): p. 1471-1483.
11. Wigbers, M.C., et al., *A hierarchy of protein patterns robustly decodes cell shape information*. Nature Physics, 2021. **17**(5): p. 578-584.
12. Turing, A.M., *The chemical basis of morphogenesis*. Philos Trans of the Royal Society B, Biological Sciences, 1952. **237**.
13. Bhattacharyya, S. and J.M. Yeomans, *Coupling Turing stripes to active flows*. Soft Matter, 2021. **17**(47): p. 10716-10722.
14. Senoussi, A., J.-C. Galas, and A. Estevez-Torres, *Programmed mechano-chemical coupling in reaction-diffusion active matter*. Science Advances, 2021. **7**(51): p. eabi9865.
15. Goehring, N.W., et al., *Polarization of PAR Proteins by Advective Triggering of a Pattern-Forming System*. Science, 2011. **334**(6059): p. 1137-1141.

16. Martin, A.C., M. Kaschube, and E.F. Wieschaus, *Pulsed contractions of an actin-myosin network drive apical constriction*. Nature, 2009. **457**(7228): p. 495-9.
17. Fernandez-Gonzalez, R. and J.A. Zallen, *Oscillatory behaviors and hierarchical assembly of contractile structures in intercalating cells*. Phys Biol, 2011. **8**(4): p. 045005.
18. Banerjee, S., M.L. Gardel, and U.S. Schwarz, *The Actin Cytoskeleton as an Active Adaptive Material*. Annu Rev Condens Matter Phys, 2020. **11**(1): p. 421-439.
19. Michaux, J.B., et al., *Excitable RhoA dynamics drive pulsed contractions in the early C. elegans embryo*. J Cell Biol, 2018. **217**(12): p. 4230-4252.
20. Nishikawa, M., et al., *Controlling contractile instabilities in the actomyosin cortex*. Elife, 2017. **6**.
21. Staddon, M.F., E.M. Munro, and S. Banerjee, *Pulsatile contractions and pattern formation in excitable actomyosin cortex*. PLoS Comput Biol, 2022. **18**(3): p. e1009981.
22. Hess, H. and J.L. Ross, *Non-equilibrium assembly of microtubules: from molecules to autonomous chemical robots*. Chem Soc Rev, 2017. **46**(18): p. 5570-5587.
23. Murrell, M.P. and M.L. Gardel, *F-actin buckling coordinates contractility and severing in a biomimetic actomyosin cortex*. Proc Natl Acad Sci U S A, 2012. **109**(51): p. 20820-5.
24. Schaller, V., et al., *Polar patterns of driven filaments*. Nature, 2010. **467**(7311): p. 73-7.
25. Sanchez, T., et al., *Spontaneous motion in hierarchically assembled active matter*. Nature, 2012. **491**(7424): p. 431-434.
26. Bate, T.E., et al., *Self-mixing in microtubule-kinesin active fluid from nonuniform to uniform distribution of activity*. Nature Communications, 2022. **13**(1): p. 6573.
27. Ross, T.D., et al., *Controlling organization and forces in active matter through optically defined boundaries*. Nature, 2019. **572**(7768): p. 224-229.
28. Lemma, L.M., et al., *Spatiotemporal patterning of extensile active stresses in microtubule-based active fluids*. PNAS Nexus, 2023. **2**(5).
29. Boujemaa-Paterski, R., et al., *Network heterogeneity regulates steering in actin-based motility*. Nat Commun, 2017. **8**(1): p. 655.
30. Guérin, C., et al., *Balancing limited resources in actin networks competition*. bioRxiv, 2024: p. 2024.09.09.612098.
31. Striebel, M., F. Brauns, and E. Frey, *Length Regulation Drives Self-Organization in Filament-Motor Mixtures*. Physical Review Letters, 2022. **129**(23): p. 238102.
32. Morozov, M. and S. Michelin, *Nonlinear dynamics of a chemically-active drop: From steady to chaotic self-propulsion*. The Journal of Chemical Physics, 2019. **150**(4).
33. Maass, C.C., et al., *Swimming Droplets*. Annual Review of Condensed Matter Physics, 2016. **7**(Volume 7, 2016): p. 171-193.
34. Jin, C., C. Krüger, and C.C. Maass, *Chemotaxis and autochemotaxis of self-propelling droplet swimmers*. Proceedings of the National Academy of Sciences, 2017. **114**(20): p. 5089-5094.
35. Hokmabad, B.V., et al., *Chemotactic self-caging in active emulsions*. Proceedings of the National Academy of Sciences, 2022. **119**(24): p. e2122269119.
36. Hokmabad, B.V., et al., *Emergence of Bimodal Motility in Active Droplets*. Physical Review X, 2021. **11**(1): p. 011043.
37. Hokmabad, B.V., et al., *Spontaneously rotating clusters of active droplets*. Soft Matter, 2022. **18**(14): p. 2731-2741.

38. Bugyi, B. and M.F. Carrier, *Control of actin filament treadmilling in cell motility*. *Annu Rev Biophys*, 2010. **39**: p. 449-70.
39. McQuillen, R. and J. Xiao, *Insights into the Structure, Function, and Dynamics of the Bacterial Cytokinetic FtsZ-Ring*. *Annual Review of Biophysics*, 2020. **49**(Volume 49, 2020): p. 309-341.
40. Yam , P.T., et al., *Actin–myosin network reorganization breaks symmetry at the cell rear to spontaneously initiate polarized cell motility*. *Journal of Cell Biology*, 2007. **178**(7): p. 1207-1221.
41. Tilney, L.G. and D.A. Portnoy, *Actin filaments and the growth, movement, and spread of the intracellular bacterial parasite, Listeria monocytogenes*. *The Journal of cell biology*, 1989. **109**(4): p. 1597-1608.
42. Marchand, J.-B., et al., *Actin-based Movement of Listeria Monocytogenes: Actin Assembly Results from the Local Maintenance of Uncapped Filament Barbed Ends at the Bacterium Surface*. *The Journal of Cell Biology*, 1995. **130**(2): p. 331-343.
43. Cudmore, S., et al., *Actin-based motility of vaccinia virus*. *Nature*, 1995. **378**(6557): p. 636-8.
44. Moore, A.S., et al., *Actin cables and comet tails organize mitochondrial networks in mitosis*. *Nature*, 2021. **591**(7851): p. 659-664.
45. van der Gucht, J., et al., *Stress release drives symmetry breaking for actin-based movement*. *Proc Natl Acad Sci U S A*, 2005. **102**(22): p. 7847-52.
46. van Oudenaarden, A. and J.A. Theriot, *Cooperative symmetry-breaking by actin polymerization in a model for cell motility*. *Nature Cell Biology*, 1999. **1**(8): p. 493-499.
47. Mogilner, A. and G. Oster, *Cell motility driven by actin polymerization*. *Biophysical Journal*, 1996. **71**(6): p. 3030-3045.
48. Mogilner, A. and G. Oster, *Force Generation by Actin Polymerization II: The Elastic Ratchet and Tethered Filaments*. *Biophysical Journal*, 2003. **84**(3): p. 1591-1605.
49. Bernheim-Groswasser, A., et al., *The dynamics of actin-based motility depend on surface parameters*. *Nature*, 2002. **417**(6886): p. 308-311.
50. H, K., et al., *Observation and kinematic description of long actin tracks induced by spherical beads*. *Biophys J.*, 2010. **99**: p. 2793-802.
51. Loisel, T.P., et al., *Reconstitution of actin-based motility of Listeria and Shigella using pure proteins*. *Nature*, 1999. **401**: p. 613-616.
52. Lambrechts, A., et al., *Listeria comet tails: the actin-based motility machinery at work*. *Trends Cell Biol*, 2008. **18**(5): p. 220-7.
53. Higgs, H.N., L. Blanchoin, and T.D. Pollard, *Influence of the C terminus of Wiskott-Aldrich syndrome protein (WASp) and the Arp2/3 complex on actin polymerization*. *Biochemistry*, 1999. **38**(46): p. 15212-22.
54. Shao, D., H. Levine, and W.-J. Rappel, *Coupling actin flow, adhesion, and morphology in a computational cell motility model*. *Proceedings of the National Academy of Sciences*, 2012. **109**(18): p. 6851-6856.
55. Singh, R., E. Tjhung, and M.E. Cates, *Self-propulsion of active droplets without liquid-crystalline order*. *Physical Review Research*, 2020. **2**(3): p. 032024.
56. Hopkins, A., et al., *Motility induced phase separation of deformable cells*. *Soft Matter*, 2023. **19**(42): p. 8172-8178.

57. Caballero, F., *cuPSS: a package for pseudo-spectral integration of stochastic PDEs*. arXiv preprint arXiv:2405.02410, 2024.
58. Boukellal, H., et al., *Soft Listeria: Actin-based propulsion of liquid drops*. Physical Review E, 2004. **69**(6): p. 061906.
59. Redner, G.S., A. Baskaran, and M.F. Hagan, *Reentrant phase behavior in active colloids with attraction*. Physical Review E, 2013. **88**(1): p. 012305.
60. Yoshinaga, N. and T.B. Liverpool, *Hydrodynamic interactions in dense active suspensions: From polar order to dynamical clusters*. Physical Review E, 2017. **96**(2): p. 020603.
61. Chen, Y.-J., Y. Nagamine, and K. Yoshikawa, *Self-propelled motion of a droplet induced by Marangoni-driven spreading*. Physical Review E—Statistical, Nonlinear, and Soft Matter Physics, 2009. **80**(1): p. 016303.
62. Fruchart, M., et al., *Non-reciprocal phase transitions*. Nature, 2021. **592**(7854): p. 363-369.
63. Mandal, R., et al., *Learning dynamical behaviors in physical systems*. arXiv preprint arXiv:2406.07856, 2024.

SUPPLEMENTARY INFORMATION

Emergence of Anti-chemotactic Flocking in Active Biomimetic Colloids

Joseph D. Lopes*,¹ Benjamin Winterstrain*,¹ Fernando Caballero,¹ Amélie Chardac,¹ Izaiah Alvarado,² Adrielle T. Cusi,¹ Shibani Dalal,¹ Gess Kelly,¹ Michael R. Stehnach,¹ Bruce L. Goode,³ Thomas G. Fai,⁴ Michael F. Hagan,¹ Michael M. Norton,¹ and Guillaume Duclos¹

¹*Department of Physics, Brandeis University, 415 South street, Waltham, MA 02453*

²*Department of Biochemistry, Brandeis University, 415 South street, Waltham, MA 02453*

³*Department of Biology, Brandeis University, 415 South street, Waltham, MA 02453*

⁴*Department of Mathematics, Brandeis University, 415 South street, Waltham, MA 02453*

I. DESCRIPTION OF THE SUPPLEMENTARY MOVIES

- **Movie S1: Flocking phase.** Time series of 6 μm -diameter beads propelled by an actin comet (phase contrast microscopy, 15X magnification, total duration: 5h).
- **Movie S2: Binary collision in the flocking phase:** 6 μm -diameter beads are propelled by an actin comet (phase contrast microscopy, 15X magnification).
- **Movie S3: Non-flocking phase.** Time series of 1.5 μm -diameter beads propelled by an actin comet (phase contrast microscopy, 15X magnification, total duration: 5h).
- **Movie S4: Binary collision in the non-flocking phase:** 1.5 μm -diameter beads are propelled by an actin comet (phase contrast microscopy, 15X magnification).
- **Movie S5: Simulation of spontaneous symmetry breaking of a single bead.** In contrast to Movies S6 and S7, we let the bead naturally initiate motion. $\tilde{R} = 12.5$, $k_1 = 1.76$, $k_2 = 59.625$, and $\tilde{D}_m = 1$, all other parameters are defined in Table S2.
- **Movie S6: Simulation of single bead motility for varying radii** $\tilde{R} = \{10, 15, 20, 25\}$, $\tilde{D}_m = 30$, and $\tilde{k}_2 = 3.3$, all other parameters are defined in Table S2. Columns from left to right are phase field ϕ , actin monomer \tilde{c}_m , and actin polymer \tilde{c}_p . An initial spot of polymer is applied to the right of the bead to initiate motion quickly, avoiding transients associated with spontaneous symmetry breaking.
- **Movie S7: Simulation of single bead motility for varying reaction rate** $\tilde{k}_2 = \{3, 5, 10, 20\}$, $\tilde{D}_m = 1.0$, and $\tilde{R} = 20$, all other parameters are defined in Table S2. Columns from left to right are phase field ϕ , actin monomer \tilde{c}_m , and actin polymer \tilde{c}_p . An initial spot of polymer is applied to the right of the bead to initiate motion quickly, avoiding transients associated with spontaneous symmetry breaking.
- **Movie S8: Simulation of multiple beads in the flocking state.** $\tilde{R} = 20$, $\tilde{k}_2 = 10.0$, and $\tilde{D}_m = 10.0$, all other parameters are defined in Table S2.
- **Movie S9: Simulation of multiple beads in the non-flocking state.** $\tilde{R} = 15$, $\tilde{k}_2 = 10.0$, and $\tilde{D}_m = 50.0$, all other parameters are defined in Table S2.

II. MATERIALS AND METHODS

A. Protein Purification

All recombinant proteins were expressed in BL21(DE3) cells from New England Biolabs. Final concentrations were measured using a linearized Bradford colorimetric assay with Bovine Serum Albumin (BSA) as a reference.

1. *Skeletal muscle actin from rabbit muscle acetone powder*

Rabbit skeletal muscle actin is purified following a protocol from Bruce Goode's lab at Brandeis University based on Spudich and Watt [1] with the following modifications. After centrifugation of the polymerized actin filaments, we resuspend the pellets in 30 mL of G-buffer (5 mM Tris HCl pH 8.0, 0.5 mM DTT, 0.2 mM ATP, 0.1 CaCl₂) supplemented with 10 mM dithiothreitol (DTT) and add them to a dounce homogenizer. The solution is dounced on ice until homogeneous. After incubating on ice for 1 hour, the solution is dounced once more before transferring into 10 kDa MWCO dialysis tubing. The sample is dialyzed for 2 days against G-buffer after which aggregates are removed by centrifugation at 265,000 x g for 30 minutes at 4°C. The final sample is then drop frozen, aliquoted, then stored at -80°C. When needed, an aliquot is removed from storage and allowed to thaw on ice overnight for use the following day.

2. *Capping protein*

Mus Musculus CapZ is purified using a DNA plasmid supplied by Antoine Jégou and Guillaume Romet-Lemonne (Addgene plasmid # 89950)[2]. The original protocol [3] utilized Ni-NTA beads which are transferred to a disposable column, but here we use an ÄKTA FPLC. After, the cells are lysed in buffer (40 mM NaH₂PO₄ pH 7.4, 500 mM NaCl, 30 mM Imidazole, 1 mM DTT, and 0.1 mM EDTA) supplemented with protease inhibitor cocktail (PIC) tablet (ThermoFisher, # A32955), DNase (New England Biolabs, M0303S), Phenylmethylsulfonyl Fluoride (PMSF, Millipore Sigma # 52332-5GM), and lysozyme (US Biologicals # L9200). Lysate is clarified and applied to a commercial 5 mL His-trap column (Cytiva) and eluted with lysis buffer with 500 mM imidazole. Protein is stored at -80°C in HEK buffer (20 mM HEPES pH 7.4, 1 mM EDTA, 50 mM KCl) with 10 mM DTT and 10% glycerol.

3. *Srv2*

His-tagged Srv2 is purified with nickel column affinity with the following modifications to the original protocol [4]. After applying the cell lysate to the nickel column, 5 column volumes of wash buffer containing 50 mM NaH₂PO₄ pH 8.0, 300 mM NaCl, 140 mM Imidazole, and 1 mM DTT is flowed over the column. Srv2 is eluted using a linear gradient from 140 mM to 250 mM imidazole. Pooled fractions are dialyzed against 20 mM Tris HCl pH 8.0, 150 mM NaCl, and 2 mM DTT overnight then drop frozen and stored at -80°C.

4. *Human Profilin-1*

Human profilin-1 is purified by affinity to poly-L-proline agarose [5]. The protocol followed is adapted from the original source above by the Mullins lab at the University of California San Francisco [6]. Cell lysate is applied to a homemade poly-L-proline sepharose column (following an online protocol written by the previously mentioned Mullins lab which follows the above source) and eluted by denaturation by 6 M urea. Pooled fractions are step-dialyzed against decreasing concentrations of urea to renature the protein. The final sample is drop frozen and stored at -80°C.

5. *Human Cofilin-1*

Recombinant untagged human cofilin-1 is purified by closely following [7] via cation and anion exchange chromatography.

6. *GFP-pVCA*

The VCA domain of the Whiskott aldrich syndrome protein is expressed tagged with a GFP molecule in BL21 DE3 cells. The plasmid also includes a His-tag. Expressed cells are lysed in lysis buffer (50 mM NaH₂PO₄, 300 mM NaCl, 10 mM Imidazole, and 5% glycerol) supplemented with 1 mM PMSF, $\frac{1}{4}$ PIC tab, 15 uL DNase, 5mg/ml lysozyme, 2 mM DTT, 0.5% triton X-100, and 1 mM MgCl₂. After clarification by centrifugation, the sample is applied to a HisTrap HP (Cytiva), washed with lysis buffer, then eluted with a linear gradient of elution buffer (lysis buffer + 500

mM imidazole). Protein is pooled, dialyzed against HEK buffer supplemented with 10% glycerol and 10 mM DTT. The sample is then aliquoted, flash frozen, and stored at -80°C .

B. GFP-pVCA coated polystyrene microspheres

Carboxylated polystyrene microspheres from PolySciences (6 μm beads at 2.6% solids cat# 07312-5, 3 μm beads at 2.7% solids cat# 17134-15, 1.5 μm beads at 2.7% solids cat# 17133-15) are washed in HEK buffer 3 times (70 μL bead stock + 30 μL HEK) by centrifugation and resuspension. After, 20 μL of this mixture is suspended in 14 μM GFP-pVCA, mixed well, and incubated on ice for 1 hour. The beads are pelleted using a small tabletop centrifuge and the supernatant is removed then replaced with HEK + 5 mg/ml BSA. This mixture is incubated for 15 minutes on ice. Then, in a similar fashion, the supernatant is replaced with HEK + 1 mg/ml BSA for storage at 4°C . Beads are used within 1 week of being made.

C. Flocking experiments

To make an active sample of self-propelled beads, two separate tubes are prepared. All the stock and working concentrations are listed in S1. The first tube contains G-buffer, G-actin, and exchange buffer (10x stock: 10 mM EGTA, 1 mM MgCl_2), which is mixed well before incubating at room temperature for at least 2 minutes. BSA and methylcellulose are added after incubation. A second tube is made with Arp2/3, profilin, cofilin, Srv2, capZ, and GFP-VCA coated beads.

The two tubes are mixed together and 20x initiation mix (40 mM MgCl_2 , 10 mM ATP, 1 M KCl) is added to initiate polymerization. After mixing the sample well, the desired volume is pipetted onto an acrylamide coated glass slide [8] and gently covered with a cover slip. We controlled the height of the sample chamber by varying the sample volume. The chamber is sealed with either UV glue or 2 part epoxy. After curing, the sample is immediately taken for imaging.

Reagent	Stock Concentration (μM)	Working Concentration (μM)
Actin	130	32
Arp2/3	20	0.213
Profilin	177	12.5
Cofilin	163	22
CapZ	166	0.187
GFP-pVCA	33	*
SrV-2	4.4	0.262
BSA	100 mg/ml	5 mg/ml
Methylcellulose	2% (w/w)	0.03%

TABLE S1. **Protein stocks and working concentrations.** Working concentrations unless otherwise noted in figures and videos. *See above protocol for coating microspheres in GFP-pVCA.

D. Viscosity experiment

Viscous media was prepared with PEO (molecular weight, 400,000 g/mol; Sigma-Aldrich) to the protein mix at 0.8% (w/v), which remain Newtonian (overlap concentration $c^*=3\%$ (w/v)). PEO solutions were mixed for 2h at 40 r.p.m. (tube rotator; Fisherbrand). Viscosity measurements for the same polymer mixture were previously reported in [9, 10].

E. Bead-boundary experiment

We designed a two-layered microfluidic device to study the interactions between motile beads and a either continuous or porous boundary. Channels for the flow chamber are cut in a thin PDMS membrane (150-200 μm thick). The

reservoir channel was made by casting PDM onto a 3D printed mold (Formlabs 3+ Resin Printer). A polyester membrane with a 0.8 μm pore size (Steritech Corporation, #PET0847100) is placed over the PDMS piece such that the PDMS forms the bottom wall of the reservoir and the membrane is cut to size. For the non-porous boundary, the protein reservoir is replaced by solid block of PDMS. The device is sealed using UV glue (Norland Optical, part 8101). Once the device is assembled, two mixtures of proteins, one with pVCA-coated beads and one without, are prepared to be loaded into the device. The sample containing beads is manually loaded into the bottom sample chamber using a syringe and needle, while the sample without beads is manually loaded into the reservoir above using a syringe and Tygon Tubing (Cole-Parmer, ID 0.01 in, OD 0.03 in, #06419-00) through the pre-punched holes on the top of the reservoir. The entire perimeter of the device including any inlets/outlets are then sealed using 2-part epoxy. A second experiment is run in parallel substituting the PDMS reservoir chip with the solid PDMS block. The filled devices are immediately taken for imaging. A control experiment is performed simultaneously in quasi-2D flow chamber to confirm that the beads are motile and flocking in 2D.

F. Microscopy

Phase contrast and fluorescence images are taken with a Nikon TE2000 inverted microscope equipped with an Andor Zyla camera. Phase-contrast images were taken at 1 or 2 images per minute with either 10x or 20x objectives with a Ph1 phase ring. High-magnification fluorescence images of the actin were taken using a 100x oil immersion objective. Data in the thick flow chambers (Fig 5) was collected using a laser scanning confocal microscope (TCSSP8, Leica Microsystems GmbH) where a 488 nm laser is used to excite GFP attached to the VCA on the surface of our polystyrene beads, a 20x air objective and 3 μm z-step. Three positions with the porous membrane boundary plus 3 positions with a non-porous membrane boundary are scanned one after another with 10 minutes between scans.

G. Data Analysis

1. Particle tracking

The colloids were segmented and tracked with a subpixel accuracy [11–13]. We define the individual colloid velocities from their displacements over two subsequent frames with time interval δt : $v_i(t) = r_i(t + \delta t) - r_i(t)$, where $r_i(t)$ and $v_i(t)$ are respectively the position and velocity of a particle i at time t .

2. Criteria to detect flocks

We define a flock as a group of at least two colloids that are close to each other and move in the same direction. In practice, we apply the following criteria to determine if two colloids i and j are flocking at time t :

- The distance between their center of mass is less than five times their radius R : $|r_i(t) - r_j(t)| < 5R$
- The difference between the orientation of their displacement is smaller than 45° : $|\theta_j(t) - \theta_i(t)| < \frac{\pi}{4}$, where $\theta_i(t)$ is the angle of the velocity $v_i(t)$.

Two colloids verifying those criteria are called neighbors. We extract the list of neighbors for each colloid and reconstruct the flocks by applying the rule: two colloids sharing the same neighbors belong to the same flock. We then assign each colloid i the size $n_i(t)$ of the flock it belongs to. $n_i(t) = 1$ for single colloids.

3. Flocking parameter

The instantaneous flocking parameter is defined as the ratio between the number of colloids belonging to a flock ($n_i(t) > 1$) and the total number of colloids in the field of view, at time t . The flocking parameter for a given experiment is the time average of the instantaneous flocking parameter.

4. Analysis of confocal data

pVCA-covered Beads in confocal image stacks are segmented using MATLAB. A threshold is applied to each confocal image, and detected objects are filtered by size such that small objects of only a few pixels are removed. Then, the circularity of each object is computed to remove irregular objects and select only the fluorescent beads in the field of view. The bead density is measured by integrating the number of beads per z-slice.

5. Measurement of exponential decay length ξ from single-bead simulations

Simulations of single motile beads reveals the spatial distribution of actin monomers around a motile bead. Such profiles are shown in Fig. 2F,G of the main text. We measured the decay length of the actin monomer concentration along the direction perpendicular to the beads' motion. The actin monomer profile is well described by a double exponential. The decay length, ξ , corresponds to the shortest of the two exponential length. The concentration profile is fitted using a non-linear squares method.

6. Statistical analysis and number of independent replicates

When appropriate, mean and standard deviations of the experimental data are shown as a disk and an errorbar (Insert of Fig. 2B and 2C). In Fig. 4H,I,J, each dot represents the time average flocking parameter for an independent experiment.

III. MODEL

We model the dynamics of polymerization-driven beads through coupled PDEs describing reaction-diffusion processes, active hydrodynamics, and phase fields for capturing bead dynamics. In this section, we first derive the model and then non-dimensionalize it using energy, time, and length scales intrinsic to the equations.

A. Free energy potentials for phase field and reactive species

A Cahn-Hilliard free energy with minima at $\phi_{\pm} = \{0, 1\}$ is used to define particle bodies

$$f_{\phi_i} = \kappa \frac{1}{2} \phi_i^2 (1 - \phi)^2 + \frac{1}{2} \gamma \nabla \phi_i \cdot \nabla \phi_i + \kappa_{\phi\phi} \sum_{j=1, i \neq j}^N \frac{1}{2} \phi_i^2 \phi_j^2 + \lambda A_0 \frac{1}{2} \left(1 - \frac{1}{A_0} \int \phi_i^2 dx \right)^2, \quad (\text{S1})$$

where the index indicates the i^{th} particle. The first two terms are the standard Cahn-Hilliard terms responsible for setting the equilibrium dense and dilute values of the field ϕ and the interface width. The third term describes steric repulsion between beads, and the final term is a Lagrange multiplier that maintains uniform bead size by penalizing deviations from A_0 . For sufficiently large λ . To approximate the impermeability of the bead surface, we include free energy terms that promote cross-diffusion between the chemical species and the phase field variables

$$f_c = \kappa_c \frac{1}{2} (c_m^2 + c_p^2) \left(1 + \sum_{i=1}^N \phi_i^2 \right). \quad (\text{S2})$$

We evolve the phase field using non-conserved gradient descent dynamics, known in the literature as model A,

$$\frac{\partial \phi_i}{\partial t} + \mathbf{u} \cdot \nabla \phi_i = - \frac{1}{\Gamma} \frac{\delta F_{\phi}}{\delta \phi_i}, \quad (\text{S3})$$

where $F_{\phi} = \int f_{\phi} dx$ and

$$\frac{\delta F_{\phi}}{\delta \phi_i} = \kappa (2\phi_i^3 - \phi_i) + \gamma \nabla^2 \phi_i + \kappa_{\phi\phi} \phi_i \sum_{j=1, i \neq j}^N \left[\phi_j^2 + \lambda \phi_i \left(1 - \frac{1}{A_0} \int \phi_i^2 dx \right) \right]. \quad (\text{S4})$$

B. Reaction-diffusion dynamics of monomer and polymer fields

We model the polymerization reaction R as a two-step process consisting of nucleation $\propto k_1$ and growth $\propto k_2$

$$R_{\text{on}}(c_m, c_p) = \left(k_1 + k_2 \frac{c_p^2}{k_d^2 + c_p^2} \right) c_m. \quad (\text{S5})$$

We model the nonlinear growth using a Hill function. This form has been used in prior works to capture cooperative growth in polymerizing actin networks and helps stabilize the simulations by preventing run-away growth.

The density of monomers and polymers (c_m and c_p) follow standard diffusive dynamics, with diffusion constants D_m and D_p respectively. They are also advected by the flow \mathbf{u} , and react through the reaction term described above, modulated by the presence of interfaces ($|\nabla\phi|^2$). Polymers also decay back to monomers at a rate k_{off} . These dynamics are contained in the following equations

$$\frac{\partial c_m}{\partial t} + \mathbf{u} \cdot \nabla c_m = D_m \nabla \cdot \nabla \frac{\delta F_c}{\delta c_m} - |\nabla\phi|^2 l_\gamma^2 R_{\text{on}} + k_{\text{off}} c_p, \quad (\text{S6})$$

$$\frac{\partial c_p}{\partial t} + \mathbf{u} \cdot \nabla c_p = D_p \nabla \cdot \nabla \frac{\delta F_c}{\delta c_p} + |\nabla\phi|^2 l_\gamma^2 R_{\text{on}} - k_{\text{off}} c_p, \quad (\text{S7})$$

and

$$\frac{\delta F_c}{\delta c_{m,p}} = \kappa_c c_{m,p} \left(1 + \sum_{i=1}^N \phi_i^2 \right). \quad (\text{S8})$$

C. Hydrodynamics of bead transport

Particle motion is driven by forces generated at the surface through polymerization. In the Stoke's limit with substrate friction, momentum balance requires

$$\nabla \cdot \sigma + f_a - \xi u = 0, \quad (\text{S9})$$

Where $\sigma = \sigma_a + \sigma_c + \sigma_u$. The capillary body force arising from the phase field interface curvature is given by

$$\sigma_c = -\gamma \sum_{i=1}^N \nabla\phi_i \otimes \nabla\phi_i, \quad (\text{S10})$$

where we've omitted terms that would only contribute to the static pressure and not materially impact the dynamics. Equivalently, $\nabla \cdot \sigma_c = \sum_{i=1}^N \phi_i \nabla \mu_i$.

The active stress from actin polymerization follows the same form as the passive surface tension and is given by

$$\sigma_a = -\alpha l_\gamma^2 R_{\text{on}}(c_m, c_p) \sum_{i=1}^N \nabla\phi_i \otimes \nabla\phi_i, \quad (\text{S11})$$

where R_{on} is the total polymerization rate from before and α is the scale with the appropriate units to convert this rate into a stress. We include the factor l_γ^2 to account for the fact that the interface width impacts the total active stress.

For $\alpha > 0$, this stress is contractile along the interface. Thus, this term can be viewed as a form of active surface tension in the bead's actin cortex whose gradients will lead to material flows. Alternatively, in this coarse-grained view, the active stress can be viewed as extensile with an axis defined by $\hat{e}_n = \nabla\phi/|\nabla\phi|$. In other words, a contractile cortex or an extensile tail are equally valid ways of interpreting this active stress. In either case, the surface normal sets the anisotropy axis of the stress. We note that similar representations of active stresses arising from surface-bound polymerization have been used in other phase field models of motility. For convenience, all of the terms together give

$$\sum_{i=1}^N \nabla \cdot [-(\alpha l_\gamma^2 R_{\text{on}}(c_m, c_p) + \gamma) \nabla\phi_i \otimes \nabla\phi_i] + \nabla^2 \mathbf{u} - \xi \mathbf{u} - \nabla P = 0. \quad (\text{S12})$$

parameter description	symbol	value
dimensionless diffusivity of actin monomers c_m	\tilde{D}_m	1-100
dimensionless diffusivity of polymerized actin c_p	\tilde{D}_p	0.1
dimensionless nucleation rate	\tilde{k}_1	0.1-2
dimensionless growth rate	\tilde{k}_2	1-20
dimensionless disassociation constant for Hill equation	\tilde{k}_d	0.3
dimensionless depolymerization rate	\tilde{k}_{off}	0.006
dimensionless polymerization stress factor	$\tilde{\alpha}$	5-30
ratio of phase field interface thickness to hydrodynamic screening length	ϵ	0.2
dimensionless bead radius	\tilde{R}	10-40
spatial domain size	$L_X \times L_Y$	$256^2 - 1024^2$
number of spatial modes	$N_X \times N_Y$	$256^2 - 1024^2$
typical time step size	Δt	0.05
typical simulation duration	T	$10^6 \Delta t$

TABLE S2. Dimensionless parameters for numerical simulations.

D. Dimensionless Equations

In order to develop a reduced set of control parameters, we non-dimensionalize our system of equations. The coupled reaction-diffusion-convection equations possess numerous time and length scales. We choose the length scale $l \sim \sqrt{\gamma/\kappa}$, which is approximately the interface width, and for the time scale, the dissipation rate from the phase field dynamics $t \sim \Gamma/\kappa$. For both c_m and c_p , we use the initial concentration $c_{m,0}$ as the concentration scale. Applying these scales to Eqn. S2 yields the dimensionless phase field dynamics:

$$\frac{\partial \phi_i}{\partial \tilde{t}} + \tilde{\mathbf{u}} \cdot \tilde{\nabla} \phi_i = -\phi_i (1 - 3\phi_i + 2\phi_i^2) + \tilde{\nabla}^2 \phi_i + \tilde{\kappa}_{\phi\phi} \sum_{j=1, i \neq j}^N \phi_i \phi_j^2 + \lambda \phi_i \left(1 - \frac{1}{\tilde{A}_0} \int \phi_i^2 d\tilde{x} \right), \quad (\text{S13})$$

where $\tilde{A}_0 = \pi \frac{R^2}{l^2 \gamma}$ is the dimensionless area of a single particle and $\tilde{\kappa}_{\phi\phi} = \frac{\kappa_{\phi\phi}}{\kappa}$ is just a ratio of energy constants. The dimensionless dynamics for monomer and polymer fields are then

$$\frac{\partial \tilde{c}_m}{\partial \tilde{t}} + \tilde{\mathbf{u}} \cdot \tilde{\nabla} c_m = \tilde{D}_m \tilde{\nabla}^2 \left(c_m \left(1 + \sum_{i=1}^N \phi_i^2 \right) \right) - |\tilde{\nabla} \phi|^2 \tilde{R}_{\text{on}} + \tilde{k}_{\text{off}} \tilde{c}_p, \quad (\text{S14})$$

$$\frac{\partial \tilde{c}_p}{\partial \tilde{t}} + \tilde{\mathbf{u}} \cdot \tilde{\nabla} c_p = \tilde{D}_p \tilde{\nabla}^2 \left(c_p \left(1 + \sum_{i=1}^N \phi_i^2 \right) \right) + |\tilde{\nabla} \phi|^2 \tilde{R}_{\text{on}} - \tilde{k}_{\text{off}} \tilde{c}_p, \quad (\text{S15})$$

$$(\text{S16})$$

where $\tilde{D} = \frac{D\Gamma\kappa c}{\gamma}$, $\tilde{k}_{\text{off}} = \frac{k_{\text{off}}\Gamma}{\kappa}$. In experiments, the Peclet number for actin monomers $\text{Pe}_m \ll 1$. For numerical convenience, we strictly enforce this limit by turning off convection in Eqn. S14 and Eqn. S15 (Note that convection of the bead remains on). The dimensionless reaction rate is

$$\tilde{R}_{\text{on}} = \left(\tilde{k}_1 + \tilde{k}_2 \frac{\tilde{c}_p^2}{\tilde{k}_d + \tilde{c}_p^2} \right) \tilde{c}_m, \quad (\text{S17})$$

with $\tilde{k}_1 = k_1 \frac{\Gamma}{\kappa}$, $\tilde{k}_2 = k_2 \frac{\Gamma}{\kappa}$, and $\tilde{k}_d = k_d/c_{m,0}$. Finally, the dimensionless Stokes momentum equation is given by

$$\sum_{i=1}^N \tilde{\nabla} \cdot \left[- \left(\tilde{\alpha} \tilde{R}_{\text{on}} + \tilde{\Gamma} \right) \tilde{\nabla} \phi_i \otimes \tilde{\nabla} \phi_i \right] + \tilde{\nabla}^2 \tilde{\mathbf{u}} - \epsilon^2 \tilde{\mathbf{u}} - \tilde{\nabla} \tilde{P} = 0, \quad (\text{S18})$$

where $\tilde{\alpha} = \frac{\alpha c_{m,0}}{\eta}$ is the dimensionless polymerization stress, $\tilde{\Gamma} = \frac{\Gamma}{\eta}$ a ratio of dissipation rates, and $\epsilon = \sqrt{\frac{\gamma}{\kappa}} \sqrt{\frac{\xi}{\eta}}$ is a dimensionless ratio between the interface thickness and the hydrodynamic screening length $\sim \sqrt{\eta/\xi}$.

E. Numerical details

We have integrated Eqns. S13-S17 numerically using a pseudo-spectral method, with standard Euler-Maruyama time stepping. We have used a publicly available software package to do so, cuPSS [14] and the code is available on github. The parameters used in the simulation are shown in Table S2.

IV. TESTING OTHER MECHANISMS THAT COULD LEAD TO FLOCKING

We considered two other possible mechanisms for flocking: hydrodynamic interactions [15] and motility-induced phase separation [16], but quickly ruled them out. We eliminated hydrodynamic interactions as the dominant interaction mode by examining the motion of small passive tracer particles in the vicinity of a motile active bead. We noted that their motion was dominated by diffusion and did not measure any hydrodynamic flows around motile active beads. We further ruled out motility-induced phase separation as long-lived flocks with only two beads were routinely observed, even in the dilute regime.

V. SUPPLEMENTARY FIGURES

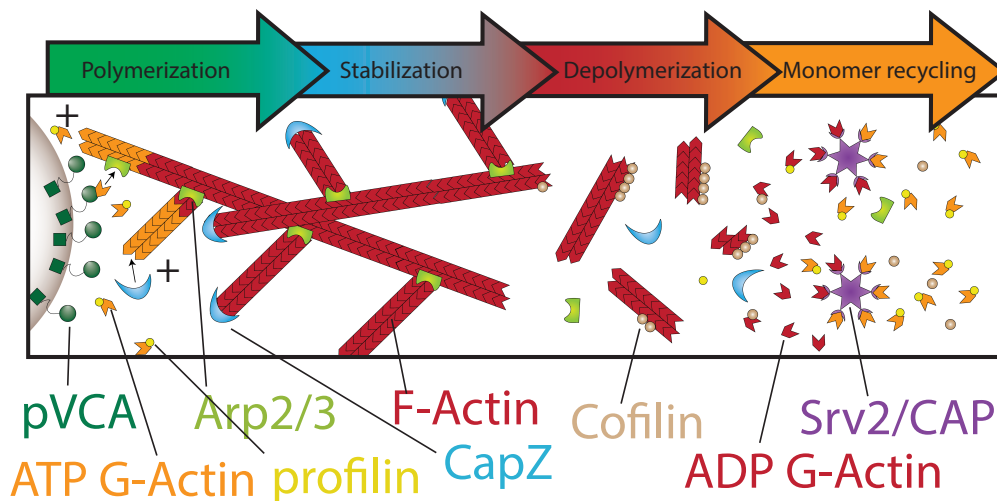


FIG. S1. **Schematic of the biochemical reactions that drive the motion of the bead.** The bead surface, covered with pVCA, is on the left of the schematic.

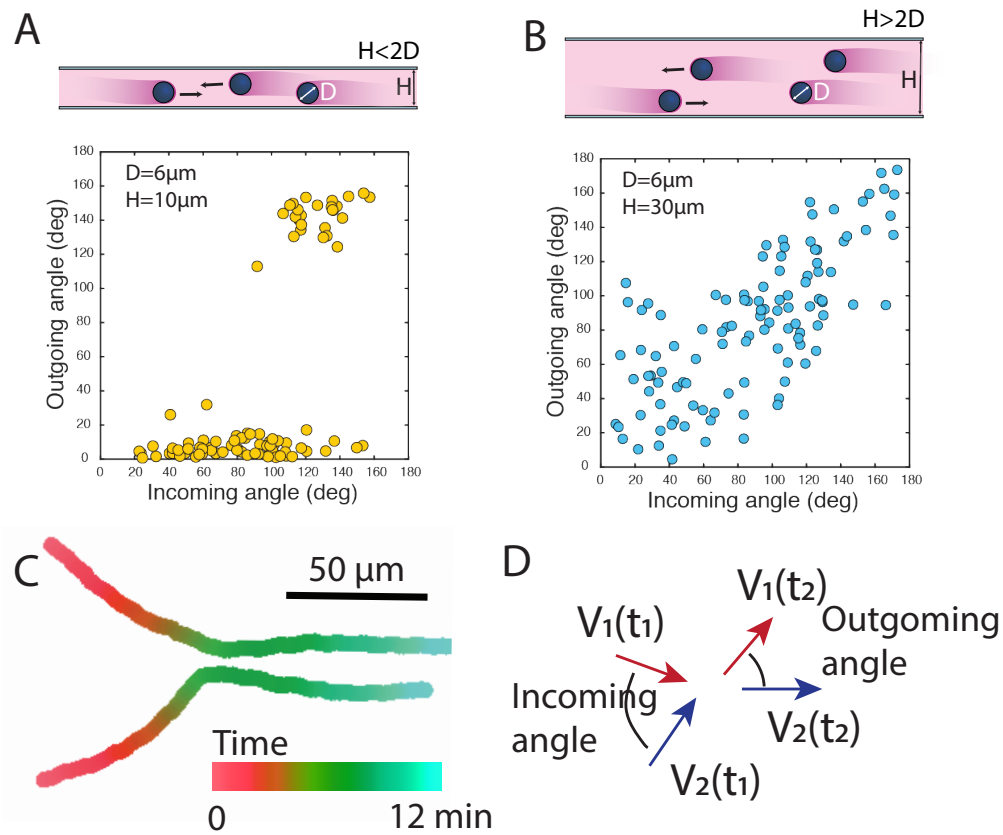


FIG. S2. **Quasi-2D confinement is necessary for flocking.** A) Plot of the velocity angles before and after collision for beads in quasi-2D chambers. Motile beads confined in quasi-2D chambers interact sterically and reorient after colliding. B) Plot of the velocity angles before and after collision for beads in 3D chambers. Motile beads in thicker chambers are able to move on top of each other. As a result, they do not reorient after colliding. C) Typical trajectory associated with panel A (beads in quasi-2D confinement, Movie S2). D) Definition of the incoming and outgoing angles.

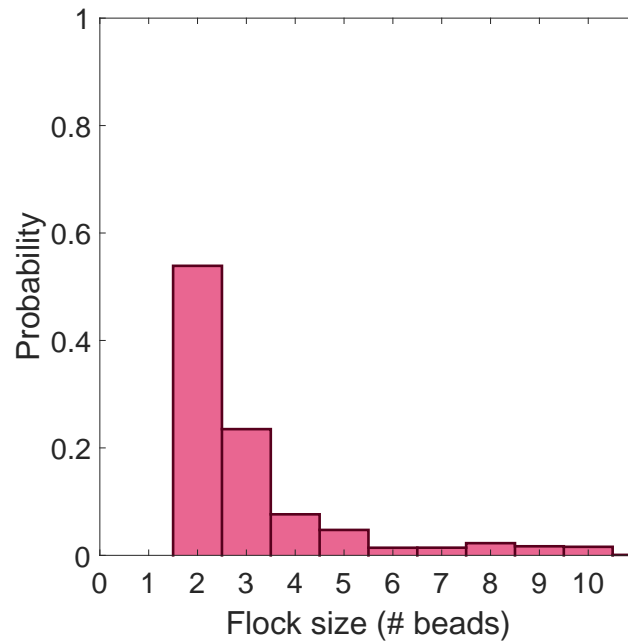


FIG. S3. **Probability distribution of the size of the flocks.** Total number of flocks analyzed ($n \geq 2$): 16890 (over 15 independent experiments, with 1000 images per experiment, beads $6 \mu\text{m}$, starting 125 min after beginning of the movies to ensure steady state regime).

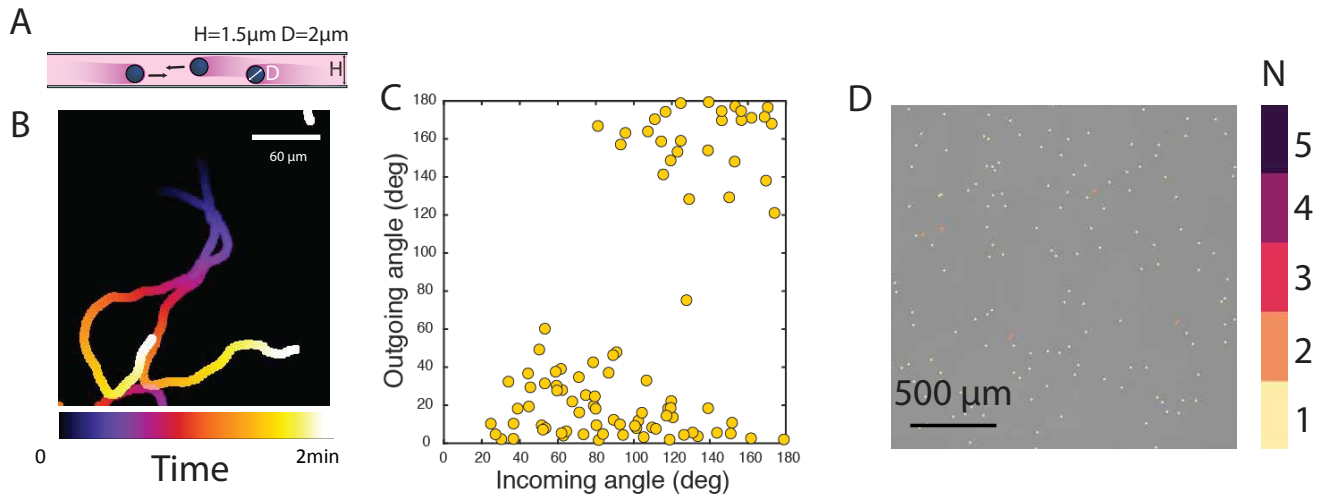


FIG. S4. **Small beads in quasi-2D chambers interact sterically but do not flock.** A) schematic of a side view of the experiment. B) time-colored trajectories of two colliding beads (Movie S4) C) Plot of the velocities angle just before and just after collision for $N=100$ binary collisions. D) Snapshot of an experiment where beads are color coded according to the size of the flock they belong to. Most of the beads move individually.

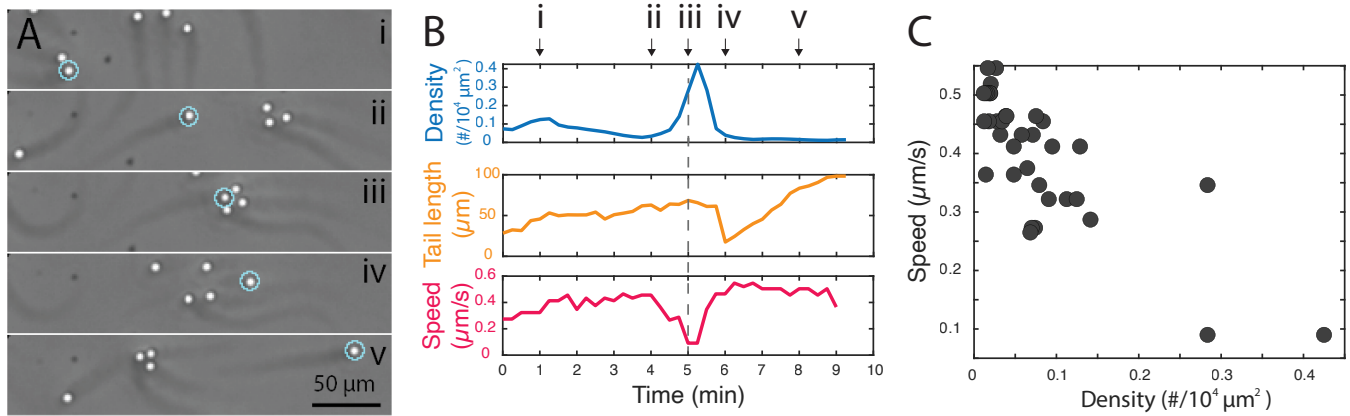


FIG. S5. **Bead speed, tail length, and tail density are impacted by local bead density.** A) Time series of a bead, marked by cyan circle, moving through a 3-beads flock. B) Time evolution of the local bead density, tail length and bead speed. C) Plot of bead speed as a function of local bead density. Beads slow down as the density increases.

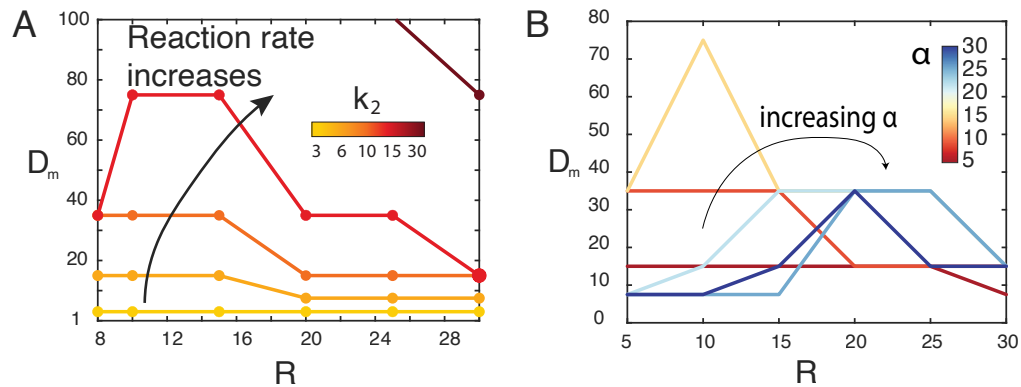


FIG. S6. **Impact of the reaction rate k_2 and the activity α on the flocking transition.** A-B) Phase boundary in the (D_m, R) phase space where A) k_2 increases and B) α increases. D_m is the diffusivity of actin monomers, R is the beads radius. The phase boundary is defined by the midpoint between a flocking and non-flocking parameter set for a given range of radii values.

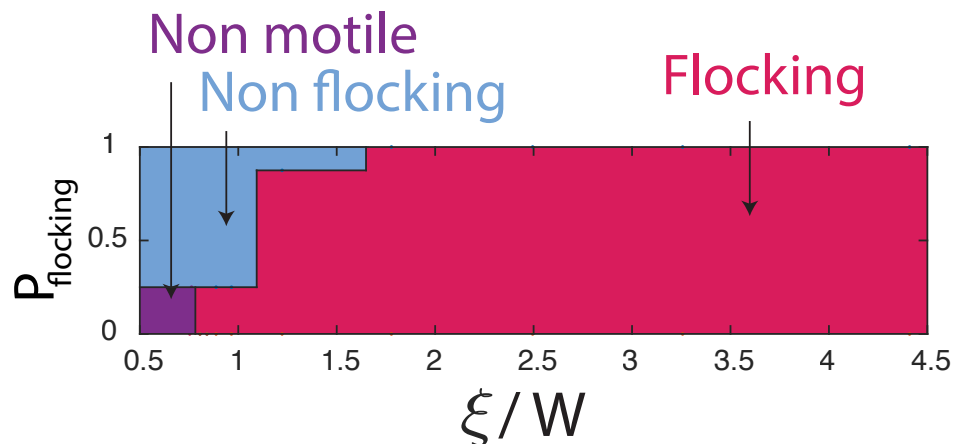


FIG. S7. **Phase behaviors as a function of the decay length of the actin monomer gradient ξ and W , the thickness of the phase field boundary.** We measured ξ from simulations of single beads. The emergent dynamics are determined by inspecting multi-bead simulations with the same parameters.

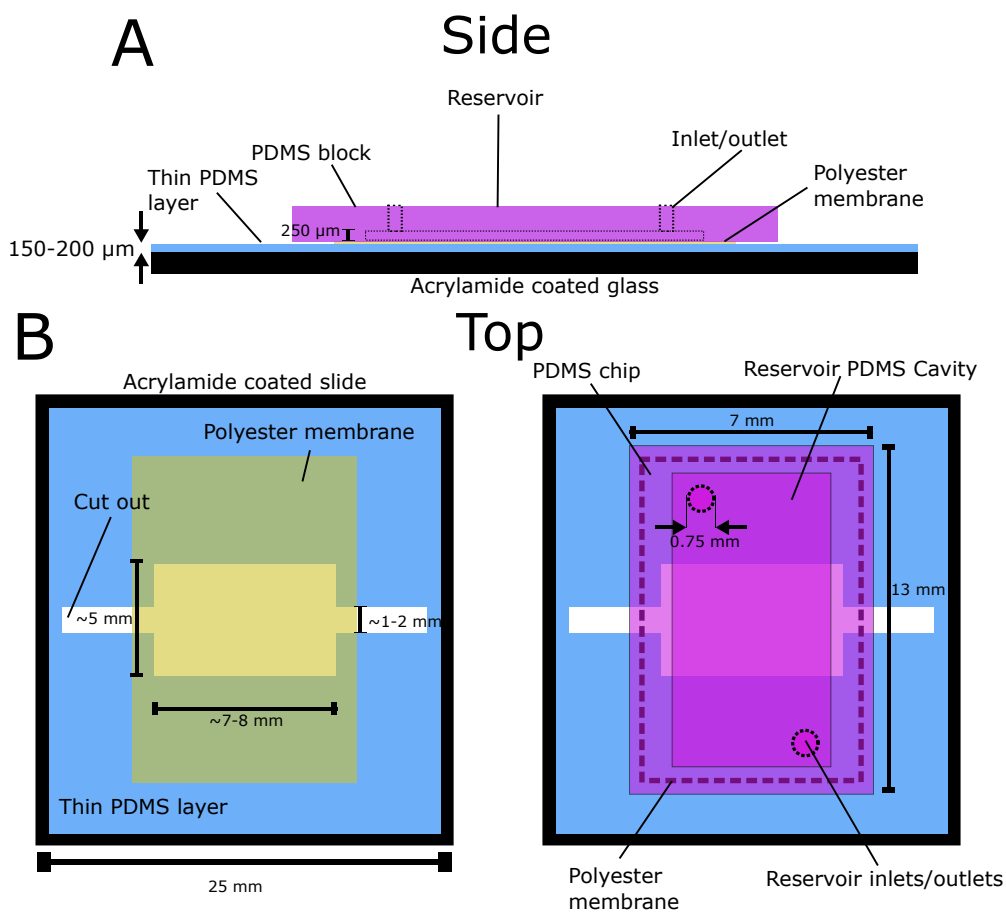


FIG. S8. **Schematic of the two-layer microfluidic device for boundary experiments.** Schematic not to scale. A) Side view of the device. The sample chamber is in the bottom blue layer while the protein reservoir is in the magenta layer. The two layers are separated by a porous membrane. Dotted lines represent the inlet and outlets in the top layer. B-Left) Top view of the sample chamber (bottom layer). A channel is cut out of a thin PDMS layer on top of a glass slide. Just above this cut out is the polyester membrane which forms the ceiling of the chamber below. The two smaller channels serve as the inlet/outlet pair to fill this chamber. B-Right) Top view of the protein reservoir (top chamber). A PDMS block with a rectangular inset sits atop the membrane such that the membrane makes up the sixth wall of the chamber. Two holes are punched through the top of the block which are the inlet/outlet pair to fill the reservoir.

-
- [1] J. A. Spudich and S. Watt, *Journal of Biological Chemistry* **246**, 4866–4871 (1971).
 - [2] S. Shekhar, M. Kerleau, S. Kühn, J. Pernier, G. Romet-Lemonne, A. Jégou, and M.-F. Carlier, *Nature Communications* **6** (2015), 10.1038/ncomms9730.
 - [3] H. Ulrichs, I. Gaska, and S. Shekhar, *Nature Communications* **14** (2023), 10.1038/s41467-023-39655-3.
 - [4] O. Quintero-Monzon, E. M. Jonasson, E. Bertling, L. Talarico, F. Chaudhry, M. Sihvo, P. Lappalainen, and B. L. Goode, *Journal of Biological Chemistry* **284**, 10923–10934 (2009).
 - [5] D. A. Kaiser, P. J. Goldschmidt-Clermont, B. A. Levine, and T. D. Pollard, *Cell Motility* **14**, 251–262 (1989).
 - [6] “Profilin Purification — Mullins Lab — mullinslab.ucsf.edu,” <https://mullinslab.ucsf.edu/profilin-purification/> (2003).
 - [7] S. Jansen, A. Collins, S. M. Chin, C. A. Ydenberg, J. Gelles, and B. L. Goode, *Nature Communications* **6** (2015), 10.1038/ncomms8202.
 - [8] T. Sanchez, D. T. N. Chen, S. J. DeCamp, M. Heymann, and Z. Dogic, *Nature* **491**, 431–434 (2012).
 - [9] M. R. Stehnach, N. Waisbord, D. M. Walkama, and J. S. Guasto, *Nature Physics* **17**, 926 (2021).
 - [10] K. W. Ebagninin, A. Benchabane, and K. Bekkour, *Journal of colloid and interface science* **336**, 360 (2009).
 - [11] P. J. Lu, P. A. Sims, H. Oki, J. B. Macarthur, and D. A. Weitz, *Optics Express* **15**, 8702 (2007).
 - [12] J. C. Crocker and D. G. Grier, *Journal of Colloid and Interface Science* **179**, 298–310 (1996).
 - [13] E. D. D Blair, “The Matlab Particle Tracking Code Respository,” <https://site.physics.georgetown.edu/matlab/index.html> (2008).
 - [14] F. Caballero, arXiv preprint arXiv:2405.02410 (2024).
 - [15] J. Toner, Y. Tu, and S. Ramaswamy, *Annals of Physics* **318**, 170 (2005), special Issue.
 - [16] M. E. Cates and J. Tailleur, *Annual Review of Condensed Matter Physics* **6**, 219 (2015).